

Influence of Evaporating Droplets in the Turbulent Marine Atmospheric Boundary Layer

Tianze Peng¹  · David Richter¹ 

Received: 23 December 2016 / Accepted: 11 July 2017 / Published online: 1 August 2017
© Springer Science+Business Media B.V. 2017

Abstract Sea-spray droplets ejected into the marine atmospheric boundary layer take part in a series of complex transport processes. By capturing the air-droplet coupling and feedback, we focus on how droplets modify the total heat transfer across a turbulent boundary layer. We implement a high-resolution Eulerian–Lagrangian algorithm with varied droplet size and mass loading in a turbulent open-channel flow, revealing that the influence from evaporating droplets varies for different dynamic and thermodynamic characteristics of droplets. Droplets that both respond rapidly to the ambient environment and have long suspension times are able to modify the latent and sensible heat fluxes individually, however the competing signs of this modification lead to an overall weak effect on the total heat flux. On the other hand, droplets with a slower thermodynamic response to the environment are less subjected to this compensating effect. This indicates a potential to enhance the total heat flux, but the enhancement is highly dependent on the concentration and suspension time.

Keywords Direct numerical simulation · Heat fluxes · Marine atmospheric boundary layer · Sea spray

1 Introduction

Characterizing and understanding the complex physical processes in which droplets participate is important for a variety of meteorological applications. In particular, despite more than 30 years of dedicated research, critical questions still remain regarding the role of spray on the air-sea transfer of heat, moisture, and momentum. Many of the basic coupling mechanisms

✉ David Richter
David.Richter.26@nd.edu

Tianze Peng
Tianze.Peng.16@nd.edu

¹ Department of Civil & Environmental Engineering & Earth Sciences, University of Notre Dame, Notre Dame, IN, USA

are still not well understood, and the potential magnitude of spray's feedback in the marine atmospheric boundary layer (MABL) remains unclear.

In general, bulk parametrizations are used as a standard tool for estimating surface fluxes in large-scale weather and climate models. For example, momentum exchange is dictated by C_D , the air-sea drag coefficient, in combination with a reference velocity (presumably at the first grid point in numerical models). Likewise, the bulk transfer coefficients C_H and C_E lead to sensible and latent heat fluxes, respectively, and are parametrized in a similar manner. Few existing measurements, particularly for the thermodynamic exchange coefficients, have been made at high wind speeds, and generally show a weak dependence of evaporation coefficients on wind speed (DeCosmo et al. 1996; Drennan et al. 2007; Zhang et al. 2008). Other indirect methods are in qualitative agreement (Bell et al. 2012; Richter et al. 2016). While these observational measurements are important for constraining the bulk coefficients, they are all too coarse-grained and do not include the influence of spray and other small-scale physical processes in the MABL.

Theoretical and numerical models, however, show that the bulk coefficients are fairly well constrained and understood at low wind speeds (e.g., Fairall et al. 1994, 2003). Recently, Andreas et al. (2015), based on earlier work (Andreas 1990, 1992, 1995), provided an improved bulk air-sea flux algorithm to that in Andreas (2005). The model partitions fluxes of heat, moisture, and momentum into the so-called "spray-mediated" and "interfacial" routes. Refined by using a large number of existing observations, the study finds that the spray route of air-sea scalar transfer becomes a significant fraction of the total at modest wind speeds, and that the spray-mediated sensible and latent heat fluxes overcome the interfacial fluxes at 19 and 26 m s⁻¹ respectively.

While the model of Andreas et al. (2015) represents the collective microphysical feedback of droplets in a bulk (i.e. one-dimensional) formulation, the alternative approach is to estimate the accumulated impact of spray by tracking droplets individually. Edson and Fairall (1994) designed a Lagrangian model to investigate the turbulent transport of evaporating droplets based on stochastically generated ambient MABL conditions. The model is then extended in Edson et al. (1996) by adding the interaction of droplets with the turbulence field as represented by a two-dimensional $k - \epsilon$ model. The results show a substantial increase in latent heat flux along with a significant decrease in sensible heat flux for droplets released at the significant wave height. Mueller and Veron (2014a, b) put forward a Lagrangian stochastic model with more sophisticated and accurate droplet physics (Mueller and Veron 2010) and an updated source function (Veron et al. 2012). The results predict that the total enthalpy coefficient quickly increases as wind speed exceeds 20 m s⁻¹ (here the enthalpy flux is defined as the sum of the sensible and latent heat fluxes). However, in typical Lagrangian stochastic models, feedback of evaporating spray with the surrounding flow is difficult to include since the fluid dynamics of the air phase is not computed directly.

Other models based on an Eulerian framework are usually cast in a one-dimensional sense, where the turbulence is modelled based on Monin–Obukhov similarity theory. In this way, vertical turbulent transport of spray is typically parametrized using an eddy diffusivity akin to passive scalar transport. Thermodynamic coupling can be included either indirectly, via spray-induced modifications to the mean profiles of humidity and temperature, or directly, via direct modifications to the fluxes themselves. In many of these models, spray has been shown to significantly modify temperature and humidity in the MABL, as well as affect the dynamics of large-scale tropical cyclones (Andreas and Emanuel 2001; Bianco et al. 2011; Bao et al. 2011; Rastigejev and Suslov 2016). Regardless of model type (i.e. Lagrangian stochastic versus one-dimensional Eulerian), it is remarkable that the numerical and theoretical studies mentioned

above share similar conclusions about the influence of spray on MABL thermodynamics, but seemingly contradict the few existing observations in terms of the bulk transfer coefficients.

To overcome some of the limitations of the aforementioned models, in particular the difficulty of including spray feedback on the surrounding flow, we use a Lagrangian droplet model two-way coupled to a high-resolution turbulent flow. This allows for a specific focus on the underlying physics behind droplet-flow interaction, particularly in regards to heat and moisture fluxes when the droplets are evaporating. The numerical methods utilized here have been successfully applied in the engineering context (Russo et al. 2014; Bukhvostova et al. 2014; Helgans and Richter 2016), and we use them to better understand surface fluxes and transport within the spray-laden MABL. We design a set of numerical experiments in turbulent open-channel flow with direct numerical simulation (DNS), where Lagrangian droplets of a specified concentration are thermodynamically coupled to the surrounding flow. While many other factors including wave breaking and droplet formation still require attention, the primary purpose of our study is to examine the fundamental influence of evaporating droplets on the heat fluxes in an idealized and isolated setting, in order to assist in the interpretation of existing theories and measurements related to spray feedback in the MABL.

2 Methodology

2.1 Overview

Our goal is to understand the thermodynamic behaviour of droplets in a turbulent boundary-layer flow from both a per-droplet and statistical perspective. We combine the advantages of several of the aforementioned models and implement an Eulerian–Lagrangian algorithm to simulate the air (“carrier”) and droplet (“dispersed”) phases simultaneously. All scales of turbulent motion in the air phase are resolved with DNS, and no turbulence modelling is required. At the same time, we also individually track and compute the trajectory, temperature, and size of individual water droplets throughout the domain. In this section, we start with the governing equations of the carrier phase and dispersed droplets, and then introduce the configuration of our numerical experiments.

2.2 Governing Equations

2.2.1 Carrier Phase

The equations describing the conservation of mass, momentum, and energy of the air phase are solved via DNS, with the mathematical description of the model identical to Helgans and Richter (2016). We take the system as neutrally stable and incompressible, since turbulence in the spray-laden regions of the MABL is primarily driven by shear. We also assume, due to the limited variation in temperature, that material properties such as viscosity and thermal diffusivity are constant and independent of temperature and humidity.

With the assumptions stated above, the governing equations of mass, momentum, temperature, and humidity for the air are given by

$$\frac{\partial u_i}{\partial x_i} = 0, \quad (1)$$

where u_i is the velocity of the air at location x_i ,

Table 1 Simulation parameters

| Parameters | Symbols | Values |
|-------------------------------|-----------|---|
| Friction Reynolds number | Re_τ | 300 |
| Schmidt number | Sc | 0.615 |
| Prandtl number | Pr | 0.71 |
| Density of air | ρ_a | 1.1 kg m^{-3} |
| Density of water | ρ_w | 1000 kg m^{-3} |
| Kinematic viscosity of air | ν_a | $1.537 \times 10^{-5} \text{ m}^2 \text{ s}^{-1}$ |
| Specific heat of air | $c_{p,a}$ | $1006 \text{ J K}^{-1} \text{ kg}^{-1}$ |
| Specific heat of water vapour | $c_{p,v}$ | $1952 \text{ J K}^{-1} \text{ kg}^{-1}$ |
| Latent heat of evaporation | L_v | $2.44 \times 10^6 \text{ J kg}^{-1}$ |
| Molecular weight of water | M_w | $0.018 \text{ kg mol}^{-1}$ |
| Molecular weight of salt | M_s | $0.0584 \text{ kg mol}^{-1}$ |
| Vertical height of domain | δ | 0.04 m |

$$\frac{\partial u_i}{\partial t} + u_j \frac{\partial u_i}{\partial x_j} = -\frac{1}{\rho_a} \frac{\partial P}{\partial x_i} + \nu_a \frac{\partial^2 u_i}{\partial x_j \partial x_j}, \quad (2)$$

where P is the pressure, ρ_a is the air density, and ν_a is the kinematic viscosity of air (see Table 1 for parameter values),

$$\frac{\partial T}{\partial t} + u_j \frac{\partial T}{\partial x_j} = \alpha \frac{\partial^2 T}{\partial x_j \partial x_j} + \frac{1}{\rho_a} S^h, \quad (3)$$

where the specific heat of air $c_{p,a}$ and thermal diffusivity $\alpha = \kappa_T / (\rho_a c_{p,a})$ are assumed constant (κ_T is the thermal conductivity of air) and S^h is the heat source due to droplets. Also,

$$\frac{\partial q}{\partial t} + u_j \frac{\partial q}{\partial x_j} = D_v \frac{\partial^2 q}{\partial x_j \partial x_j} + \frac{1}{\rho_a} S^q, \quad (4)$$

where the diffusivity of vapour D_v is also assumed constant, the specific humidity q is defined as the ratio of local vapour density to dry air density $q = \rho_v / \rho_a$, and the source S^q is the droplet source of humidity.

2.2.2 Dispersed Phase

The diameters of most droplets near the air-sea interface are smaller than the Kolmogorov length scale η_K , the smallest scale in turbulent flow. Therefore we employ the point-particle approach, which represents droplets as infinitesimal points exhibiting their own velocity, temperature, and radius. Under the point-particle approximation, we introduce the Lagrangian equations governing the location, velocity, temperature, and radius of each particle based on the conservation of mass, momentum, and energy. The evolution of a droplet's location is computed via its velocity

$$\frac{dx_{p,i}}{dt} = v_{p,i} \quad (5)$$

where $x_{p,i}$ is the location of a particle (this does not necessarily coincide with the grid used to solve the air-phase equations), and $v_{p,i}$ is the velocity of an individual droplet. The droplet

velocity is governed by momentum conservation assuming Stokes drag with a small Reynolds number correction (Clift et al. 1978)

$$\frac{dv_{p,i}}{dt} = \left(1 + 0.15Re_p^{0.687}\right) \frac{1}{\tau_p} (v_{f,i} - v_{p,i}) - g_z \delta_{i3}, \tag{6}$$

where the particle Reynolds number is defined as $Re_p = d_p |v_{f,i} - v_{p,i}| / \nu_a$, and $\tau_p = \rho_p d_p^2 / (18 \nu_a \rho_a)$ is the acceleration time scale of the particle, which is a function of the droplet diameter d_p and droplet density ρ_p . The term g_z is the magnitude of acceleration due to gravity in the z -direction. Equation 6 indicates that a particle is accelerated both by hydrodynamic drag and gravity. The former is based on the difference of the particle velocity and the local fluid velocity $v_{f,i}$, and $v_{f,i}$ must be interpolated to the particle location from the velocity u_i in Eq. 2 at the surrounding grid points.

The thermodynamic evolution of a droplet includes both mass and temperature changes. The microphysical model used to describe droplet evaporation is based on Andreas (1992), Andreas et al. (1995), Pruppacher and Klett (1997), and Mueller and Veron (2010). A full description can be found in Helgans and Richter (2016).

We have the following equations for the mass (m_p) and radius (r_p) of a spherical droplet,

$$\frac{dm_p}{dt} = 4\pi r_p^2 \rho_w \frac{dr_p}{dt}, \tag{7}$$

$$\frac{dr_p}{dt} = \bar{h}_m \frac{\rho_a}{\rho_w} (q_f - q_p), \tag{8}$$

where ρ_w is the density of pure water. The term \bar{h}_m is the convective mass transfer coefficient of evaporative droplets

$$\bar{h}_m = \frac{1}{9} \frac{Sh_p}{Sc} \frac{\rho_p}{\rho_a} \frac{r_p}{\tau_p}, \tag{9}$$

where Sh is the Sherwood number $Sh = 2 + 0.6Re_p^{1/2} Sc^{1/3}$ (Ranz and Marshall 1952), and $Sc = \nu_a / D_v$ is the Schmidt number that relates the viscosity and vapour diffusivity (the values are given in Table 1).

Equation 8 shows that the change in particle mass (radius) is dependent on the difference between the local air humidity q_f (interpolated from the grid) and the humidity near the droplet surface q_p . The value of q_p is based on the saturation vapour pressure at the droplet temperature T_p , the surface curvature, and the droplet salinity. The detailed expression can be found in Helgans and Richter (2016), and is the same as that used in Mueller and Veron (2010).

Energy conservation governs the temperature of the droplet, which we assume uniform throughout its interior. Temperature evolution is based on the air-droplet sensible and latent heat transfer exchange rates \dot{Q}_{conv} and \dot{Q}_{latent} , the former being driven by the difference between the droplet temperature T_p and the surrounding air temperature T_f . The latter is associated with evaporation/condensation

$$\begin{aligned} \frac{dT_p}{dt} &= \frac{1}{\rho_w V_d c_L} [\dot{Q}_{conv} + \dot{Q}_{latent}] \\ &= \left[-\frac{1}{3} \frac{Nu_p}{Pr} \frac{c_{p,a}}{c_L} \frac{\rho_p}{\rho_w} \frac{1}{\tau_p} (T_p - T_f) \right] + \left[3L_v \frac{1}{r_p c_L} \frac{dr_p}{dt} \right], \end{aligned} \tag{10}$$

where V_d is the volume of the spherical water droplet, ρ_p is the bulk density of the saline droplet (nearly equal to the pure water density ρ_w), c_L is the specific heat of liquid water

(assumed constant), and L_v is the latent heat of evaporation. Sensible heat transfer between the droplet and surrounding air is treated as a convective process with a heat transfer coefficient given in non-dimensional form by an empirical relation for the Nusselt number (Ranz and Marshall 1952): $Nu_p = 2 + 0.6Re_p^{1/2}Pr^{1/3}$. Here, $Pr = \nu_a/\alpha = 0.71$ is the Prandtl number of air, which is the ratio of the viscosity and thermal diffusivity.

2.2.3 Two-Way Coupling

A key feature of our model is that it captures two-way coupling between the droplets and air—a process that nearly all past Lagrangian studies lack (Edson and Fairall 1994). We remove air-droplet momentum exchange from the formulation to specifically focus on thermodynamic coupling.

The two-way exchange of heat and moisture is found in the terms S^h and S^q in Eqs. 3 and 4. These source terms are computed at a grid node as the summation of weighted contribution from all particles that reside in the eight surrounding computational grid volumes. Detailed expressions of S^h and S^q can be found in Helgans and Richter (2016).

2.2.4 Droplet Evaporation Time Scales

To characterize the speed and extent of the evaporation of droplets, Andreas (1990) defined the characteristic temperature evolution time scale of droplets, τ_T , which is the e -folding time for a droplet reaching its equilibrium temperature (T_{eq}) from its initial temperature ($T_{p,init}$), i.e.,

$$\frac{T_p(t) - T_{eq}}{T_{p,init} - T_{eq}} = \exp\left(-\frac{t}{\tau_T}\right). \quad (11)$$

Similarly, the characteristic time scale of radius change τ_r is defined as

$$\frac{r_p(t) - r_{eq}}{r_{p,init} - r_{eq}} = \exp\left(-\frac{t}{\tau_r}\right), \quad (12)$$

where the evolution of r_{eq} is the equilibrium radius for droplets with the initial radius $r_{p,init}$.

These time scales, τ_T and τ_r , characterize the thermodynamic inertia of droplets, and Andreas (1992) indicates a gap of three orders of magnitude between the two time scales—i.e. $\tau_r/\tau_T \approx O(10^3)$ [also see Veron (2015)], showing that droplets change temperature first before a significant change in their radius due to evaporation. We take the ratio ≈ 1800 .

2.2.5 Heat Fluxes

Heat fluxes quantify the energy transfer across the boundary layer. Here we define the heat-flux components in a similar way as Richter and Sullivan (2014) and Helgans and Richter (2016), in that we define a total moist enthalpy as being the enthalpy contained by both the vapour and air phases

$$h_{gas} = \rho_a c_{p,a} T + \rho_a q (c_{p,v} T + h_v^0). \quad (13)$$

Then, with Eqs. 3 and 4, an equation for total enthalpy can be established (see Helgans and Richter 2016 for the full expression). Using this expression, we apply a Reynolds decomposition on the temperature T , moisture q , and velocity u_i of the air phase, and then average

the equation horizontally. This procedure yields a total moist enthalpy flux in the vertical direction that has the form

$$H_{total} = H_{a,total} + H_{q,total} = \text{constant}, \tag{14}$$

where $H_{a,total}$ and $H_{q,total}$ are individually decomposed into three components representing the turbulent, diffusive, and particle-induced flux of enthalpy

$$\begin{aligned} H_{a,total} &= H_{a,turb} + H_{a,diff} + H_{a,part} \\ &= \rho_a c_{p,a} \langle w' T' \rangle - \rho_a c_{p,a} \alpha \frac{d\langle T \rangle}{dz} - \int_0^z S^h dz, \end{aligned} \tag{15}$$

and

$$\begin{aligned} H_{q,total} &= H_{q,turb} + H_{q,diff} + H_{q,part} \\ &= (c_{p,v} + h_v^0) \left[\langle w' q' \rangle - \rho_a D_v \frac{d\langle q \rangle}{dz} - \int_0^z S^q dz \right]. \end{aligned} \tag{16}$$

We define positive fluxes upwards. It was shown in Helgans and Richter (2016) that cross-coupling terms between latent (we define here as terms with subscript “ q ”) and sensible (subscript “ a ”) terms are negligible and are therefore not included in the above equations. In the present study, we are ultimately interested on the role of evaporating droplets in altering these modes of enthalpy flux.

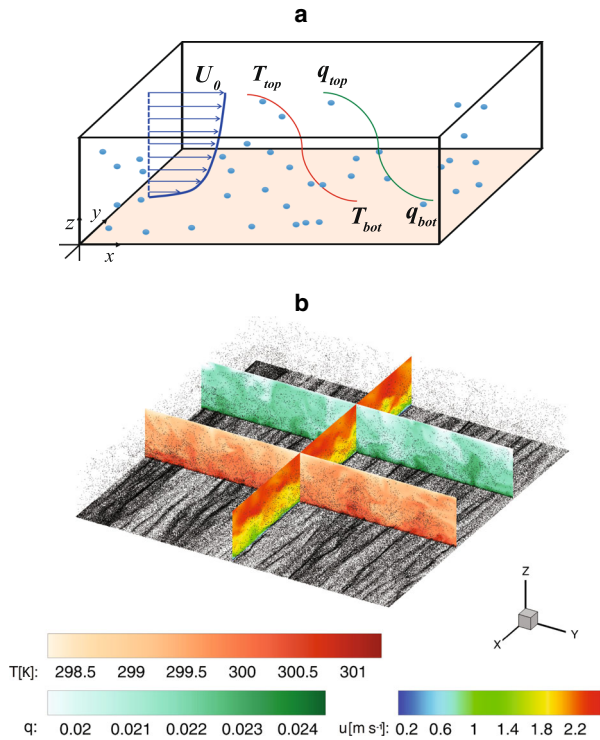
2.3 Numerical Set-Up

We use the same underlying code as in previous studies (Helgans and Richter 2016; Richter 2015; Richter and Sullivan 2014) for solving Eqs. 1–10. The solver for the carrier phase uses a pseudospectral spatial discretization with anti-aliasing in the periodic streamwise (x) and spanwise (y) directions, and uses a second-order finite difference method in the wall-normal (z) direction. Incompressibility is enforced by solving a pressure Poisson equation, while time integration is performed with a low-storage third-order Runge–Kutta method (Spalart et al. 1991) for both phases.

The domain is set up to simulate pressure-driven, turbulent open-channel flow over a flat plate. The domain has dimensions of $[2\pi\delta, 2\pi\delta, \delta]$ using a corresponding grid of $[128, 256, 128]$ grid points, where $\delta = 0.04$ m. The friction Reynolds number $Re_\tau = u_*\delta/\nu = 300$ throughout, where the friction velocity $u_* = \sqrt{\tau_w/\rho_a}$ is defined using the total stress τ_w at the bottom boundary. All simulations are initialized with a previously obtained particle-free turbulent flow field. A no-slip condition at the bottom surface and a no-stress (full-slip) condition at the top surface are enforced for the air velocity. The air temperature and humidity are specified at both the top and bottom boundaries, where the baseline condition is such that the top boundary is cooler and drier ($T_{top} = 25^\circ\text{C}$, $RH_{top} = 90\%$, where RH is the relative humidity) while the lower boundary is warmer and saturated ($T_{bot} = 28^\circ\text{C}$, $RH_{bot} = 100\%$), in order to represent a turbulent boundary layer over a smooth water surface. See Fig. 1a for a schematic, and Fig. 1b for an instantaneous temperature and humidity distribution.

At the top boundary, droplets reflect elastically in order to keep them contained within the computational domain (this is equivalent to a no-flux condition), and since particles undergo gravitational settling, they are removed from the system when they fall beneath the bottom surface. We maintain a constant loading of droplets by re-injecting a droplet for every one that is removed. The new droplets are introduced at a random location across the bottom surface and given a random initial velocity chosen from a uniform distribution between

Fig. 1 **a** A schematic of the domain, **b** an instantaneous snapshot of the domain, where the open-channel flow is driven by a pressure gradient in the x -direction that generates shear-driven turbulence. Contours of velocity, temperature, and humidity are plotted with the presence of water droplets (*black dots*) interacting with turbulent temperature and humidity fields. The number of droplets is held constant by the re-injection mechanism



zero and the velocity that would allow the droplet to reach a height of $\delta/8$ in quiescent conditions. This process mimics a high-concentration “spray-layer” near the bottom surface, and is sufficiently deep such that turbulence can entrain droplets from within this layer and transport them throughout the domain. Particles above a height of $z = \delta/8$ have necessarily been carried there by turbulent motions.

Finally, we note several important considerations regarding the dimensional quantities used. Since DNS cannot be used to simulate the true MABL, our goal here is to match as many key non-dimensional quantities as possible. For instance, our Reynolds number of $Re_\tau = 300$, while necessarily low to resolve all scales of motion, is sufficiently high so as to provide insight into the consequences of turbulent suspension and thermodynamic coupling between droplets and air.

Other quantities, such as the gravitational acceleration g_z , are chosen to provide the same non-dimensional quantities as found in the true MABL. To ensure that the droplets settle with the same tendency relative to turbulence intensity, g_z is chosen such that the non-dimensional settling velocity w_s/w' , where w' is the root-mean-square of the vertical velocity fluctuations (on the order of 1 m s^{-1} in the atmosphere) and $w_s = \tau_p g_z$ is the terminal velocity of droplets on the order of 1 m s^{-1} for a $100\text{-}\mu\text{m}$ droplet in quiescent air, see Veron (2015), is the same as that outside. Thus, we set $g_z = 0.84 \text{ m s}^{-2}$ in the present simulations.

Likewise, the droplet diameters and densities are chosen to match the dimensionless Stokes numbers of real spray droplets, $St = \tau_p/\tau_K$, where τ_K is the vertically-averaged Kolmogorov time scale of the flow. St provides an indication on how rapidly the droplet adjusts to the local air velocity. The present simulations are configured so that the Kolmogorov time scale in the simulations roughly matches that of the true MABL 2 ms is selected as a reference

value while τ_K ranges from 0.2 ms to 6.5 s (Thorpe 2005). Therefore the droplet sizes and density are chosen to match those of realistic spray as well ($\rho_p = 1000 \text{ kg m}^{-3}$, with r_p ranging between 25 and 200 μm).

Within the broad spectrum of spray droplet and aerosol sizes, which ranges from sub-micron to several millimetres (see e.g. de Leeuw et al. 2011 or Veron 2015), the radii listed above fall in the range of medium to large. Therefore references to “small”, “medium”, and “large” herein refer to the relative size of droplets within the upper portions of the full spectrum. Droplets (e.g. spume droplets) in this range not only occur at the peak of the volume spectra at high wind speeds (Fairall et al. 2009), but also dominate the heat and mass transfer. According to spray-mediated flux models, the peaks of sensible and latent heat fluxes at high wind speed are located near $r_p \approx 50$ and 100 μm respectively (Andreas 1992; Andreas et al. 2008). Therefore, we focus our selection of droplets to cover the range that most significantly influences heat and mass transfer.

3 Results and Discussion

Based on the methodology discussed above, we conduct three sets of numerical experiments (see Table 2) focusing primarily on the influence of droplet radius on overall vertical sensible and latent heat transfer (group A); additional tests are chosen to probe the sensitivity of these results to mass loading (group B) and boundary conditions (group C). Here we define the mass loading as the ratio of the mass of water and mass of air in the domain ($\Phi_m = m_w/m_a$). In this section, we compare horizontally- and time-averaged quantities (e.g., heat fluxes) with respect to droplet-free flow, and use droplet lifetime statistics to comment on the behaviour of droplets.

3.1 Influence of Droplet Size

3.1.1 Droplet Sizes

Our overall interest lies in the thermodynamic influence of droplets on mean vertical energy transfer in a turbulent boundary-layer flow. In this context, previous studies (Andreas 1990, 1992, 1995) have provided an extensive theoretical description of droplet dynamics and thermodynamics, which have indicated that droplet size is an important quantity since it controls the droplet lifetime, inertia, settling velocity, and the time scales associated with heat transfer and evaporation. We therefore construct the first group of simulations to investigate the role of droplet size on heat-flux modification by choosing six different radii: 25, 50, 75, 100, 150, and 200 μm . The selection of radii gives thermodynamic time scales τ_T ranging between 7.5 ms (25 μm) and 478.8 ms (200 μm). All other parameters are set based on Table 2.

Table 2 List of simulation groups

| Group | r_p | Φ_m | T_{top} (K) | T_{bot} (K) | RH_{top} (%) | RH_{bot} (%) |
|-------|--------|----------|-----------------------|---------------|----------------|----------------|
| A | Varied | 1% | 298.15 | 301.15 | 90 | 100 |
| B | Fixed | varied | 298.15 | 301.15 | 90 | 100 |
| C | Fixed | 1% | Systematically varied | | | |

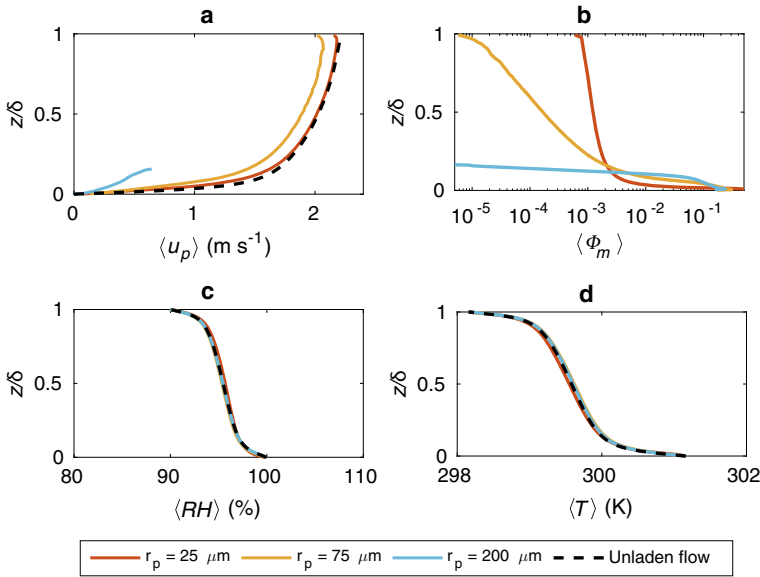


Fig. 2 Overview of the mean flow quantities for the unladen and selected laden cases from group A: **a** mean velocity of droplet phase (*solid lines*) and air phase (*dashed line*, which is equivalent to unladen flow); **b** horizontally averaged mass concentration, $\Phi_m = m_w/m_a$; **c** mean relative humidity (RH); **d** mean temperature. *Angular brackets* denote the horizontal averaging

An overview of key mean flow quantities is given in Fig. 2, where it is clear that droplets can have a significantly different mean velocity than the surrounding flow at a given height. The smallest droplets (here 25- μm diameter) behave somewhat like fluid tracers, while the largest droplets (200- μm diameter) have little correspondence to the ambient flow. This is particularly clear in Fig. 2b, where small droplets spread evenly throughout the upper domain, while large droplets, due to their high inertia and settling velocity, remain near the bottom. Figure 2c, d show that despite two-way coupling in humidity and temperature, at a mass fraction of $\Phi_m = 1\%$ only a slight change in the average fields is found for all droplet radii compared to the unladen field. If anything, large droplets slightly increase the air temperature while small droplets decrease the temperature, a feature qualitatively consistent with other studies of spray thermodynamic effects (e.g. Bianco et al. 2011).

Since the droplets are evaporating, it is important to understand their thermodynamic evolution as well. To do this, we compare the dynamic and thermodynamic evolution of representative 25- μm and 200- μm droplets in Fig. 3. Two scenarios are considered: one where the droplet has escaped the lower regions of the flow (this only occurs for the smaller droplet) and one where the droplet has a much shorter lifetime because it is transported immediately downwards after injection.

In the first of these two scenarios (first column), droplets experience evaporative cooling as they almost continuously find themselves cooler than their environment (second row). Additionally, droplets experience a vapour pressure deficit at the surface (third row) and thus evaporate with a 2% radius decrease (fourth row). However, other small droplets are transported back into the lower boundary and slightly condense and warm in their short lifetime, which leads to the next scenario.

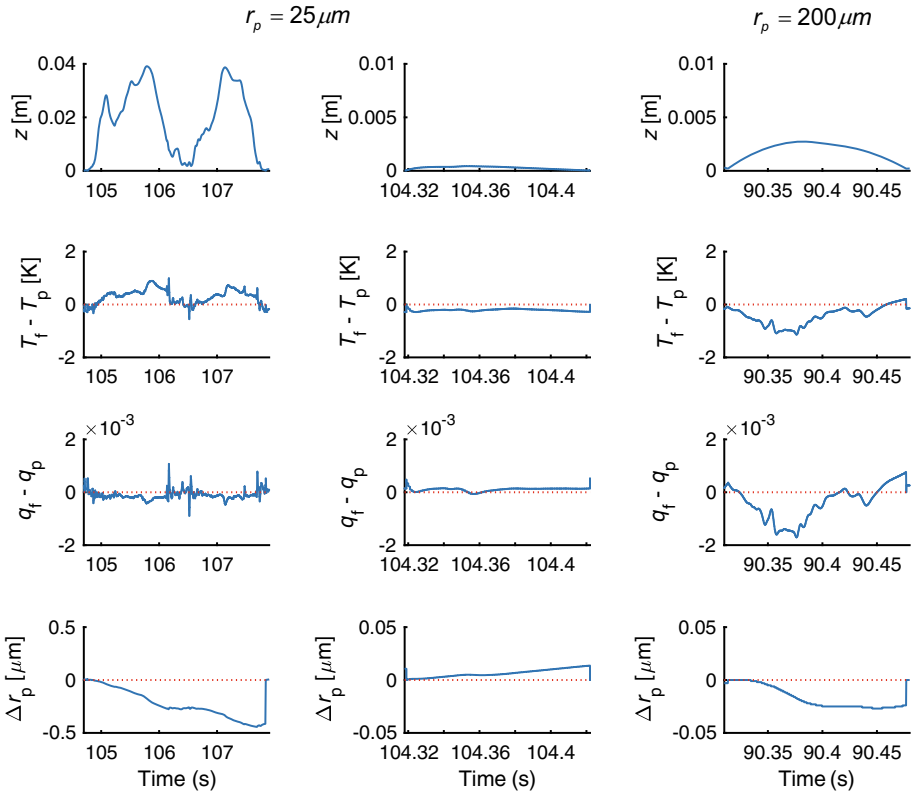


Fig. 3 Time series evolution for 25- μm (column 1 and 2) and 200- μm (column 3) droplets for various quantities: vertical location (first row), particle temperature difference from ambient (second row), specific humidity difference (third row), and radius change from inception (fourth row)

In the second scenario (second and third columns), droplets are immediately removed but due to different mechanisms: gravitational settling for large droplets and turbulent advection for small droplets. Small droplets (second column), travelling within a very limited vertical distance where local humidity is high, find themselves warmer than their surroundings due to condensation in their brief lifetime. Larger droplets, on the other hand, have a longer thermodynamic response time; therefore a lag exists in their radius change. The droplets start to evaporate because the larger inertia keeps the droplets moving further, and the droplets experience a wider range of temperature and humidity differences with the surroundings. For this scenario, we note that both small and large droplets have the potential to slightly warm the ambient air (as droplets are warmer than air). This has been seen in, e.g., Edson et al. (1996), for the release of sensible heat from droplets at high relative humidity. In Bianco et al. (2011), it is also mentioned that large droplets have the potential to warm the surrounding air due to their long thermodynamic characteristic time.

3.1.2 A Statistical View

For a better understanding of the collective effect of droplets, we track several key statistics related to the initial and terminal states. Figure 4 describes the probability density functions

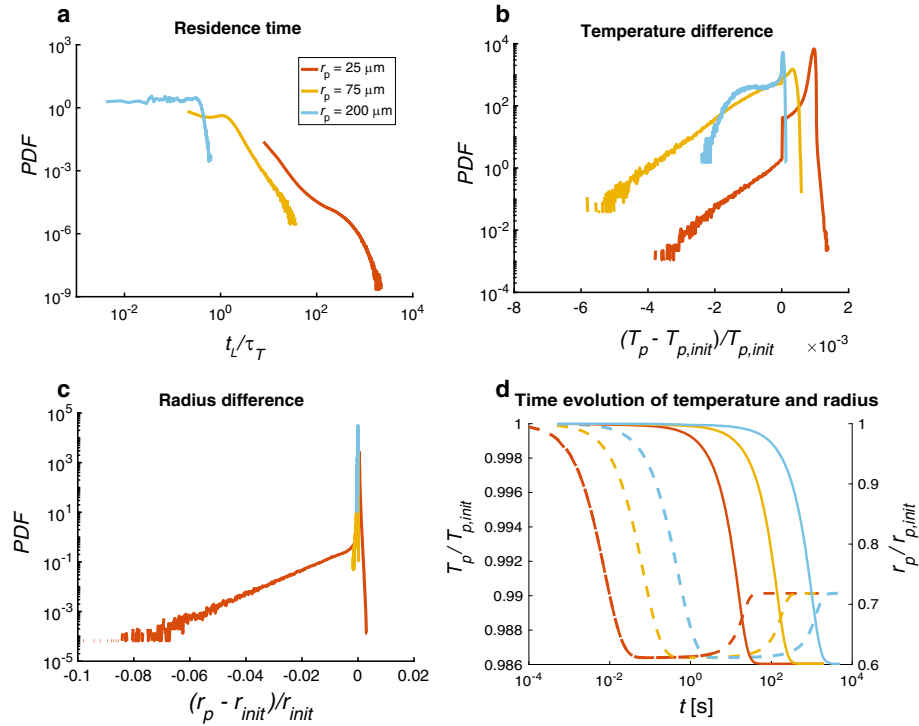


Fig. 4 Probability density functions (PDFs) of **a** normalized residence time (t_L), where temperature time scales τ_T for droplets are 0.0075 s (25 μm), 0.0670 s (75 μm), 0.4788 s (200 μm), **b** temperature difference (normalized by its initial temperature), and **c** radius difference (normalized by its initial radius) through their lifetime, compared with **d** time evolution of temperature and radius compared to their initial values during quiescent evaporation ($T_f = 298.15$ K, $T_{p,init} = 301.15$ K, $RH = 90\%$). Three types of droplets are presented: *small* (25 μm, red), *medium* (75 μm, yellow), and *large* (200 μm, blue)

(PDFs) of, (a) the normalized residence time t_L , (b) temperature change, and (c) radius change throughout the lifetime of small (25 μm), medium (75 μm), and large (200 μm) water droplets. We also plot the solutions for the temporal evolution of temperature (dashed) and radius (solid) (Eqs. 11, 12) for the three radii in Fig. 4d in quiescent ambient conditions. The gaps between solid and dashed lines of the same colour show the discrepancy between τ_T and τ_r .

We find in Fig. 4a that the droplet residence time (t_L) sharply decreases with radius. Since $\tau_T \propto r_p^2$, small droplets have sufficient time to change temperature (T_p) during their lifetime and adjust themselves to the ambient temperature (T_f). In contrast, large droplets only experience very early stages of the evolution depicted in Fig. 4d, where the temperature changes relative to the initial temperature ($T_{p,init}$) stay within a narrow range due to their short residence time and large thermal inertia. Specifically, in Fig. 4b, the discontinuity around the point where $T_p - T_{p,init} = 0$ demonstrates the rapid adjustment for small droplets, showing that small droplets either cool due to evaporation or warm from condensation when colliding with the boundary. However, large droplets essentially are all cooled by a small amount from evaporation, as noted in Fig. 3.

Regarding the change in droplet radius, Fig. 4c shows an agreement with Fig. 4b that the majority of small droplets re-enter the lower boundary at a slightly larger radius than their

initial radius (also see Fig. 3), while the exponential tail of 25 μm describes the longer suspension by turbulence entrainment. This results in up to a 2 μm decrease in radius throughout their lifetime due to evaporative cooling.

3.1.3 Enthalpy Flux

To understand how droplets modify the total heat transfer, we are particularly interested in the fluxes of both sensible and latent heat. Therefore based on Eqs. 14–16, we plot the enthalpy fluxes in Fig. 5. Figure 5a, b compare the six components and total enthalpy flux profiles for an unladen flow and a laden case with 25- μm droplets. Due to the no-penetration conditions at the top and bottom boundaries ($w = 0$), the turbulent fluxes are zero at these two locations. Likewise the particle fluxes are zero at the top boundary because the concentrations approach zero. Furthermore, the total enthalpy flux H_{total} is uniform with height, as are the total sensible and latent fluxes, respectively $H_{a,total}$ and $H_{q,total}$. Compared with the unladen case, several terms are modified by 25- μm droplets, including $H_{a,part}$, $H_{q,part}$, and $H_{q,turb}$, while the overall modification on total enthalpy flux is not as significant as its components.

Figure 5c presents the evolution of the the total enthalpy flux as a function of the droplet radius. Although the total enthalpy flux is uniform with height, in the following discussion, it is convenient to describe the magnitude of various flux components at a specific height. For this purpose we use the height at $z = \delta/8$, since this is the maximum height droplets can

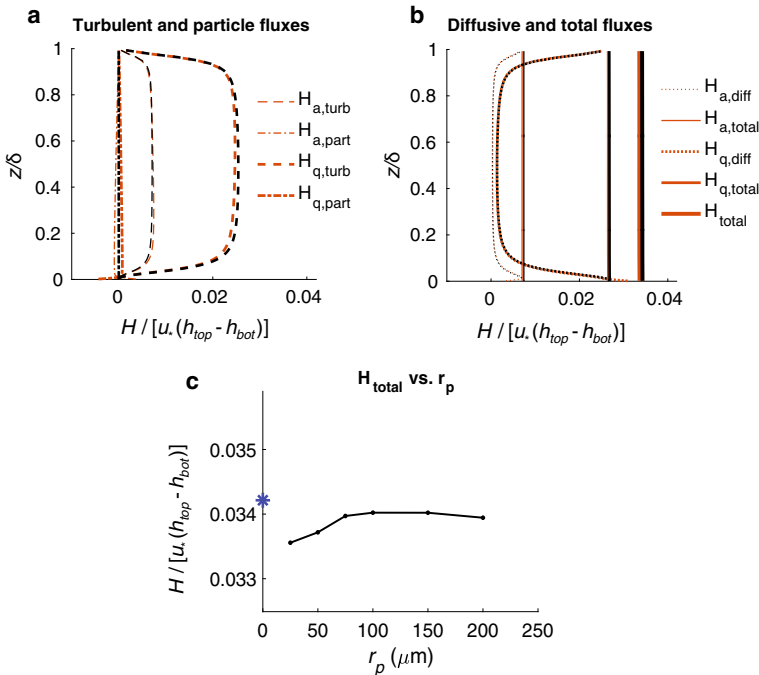


Fig. 5 Normalized vertical enthalpy fluxes for the 25- μm case (brown) and unladen case (black): **a** Turbulent and particle enthalpy fluxes, **b** diffusive and total enthalpy fluxes. Components of enthalpy flux are normalized by $u_*(h_{bot} - h_{top})$, where h_{bot} and h_{top} are calculated based on Eq. 13 given the specific humidity and temperature, and u_* is the friction velocity at lower boundary. **c** Total enthalpy flux extracted at the top of the spray layer versus particle radii. Asterisk indicates the unladen value

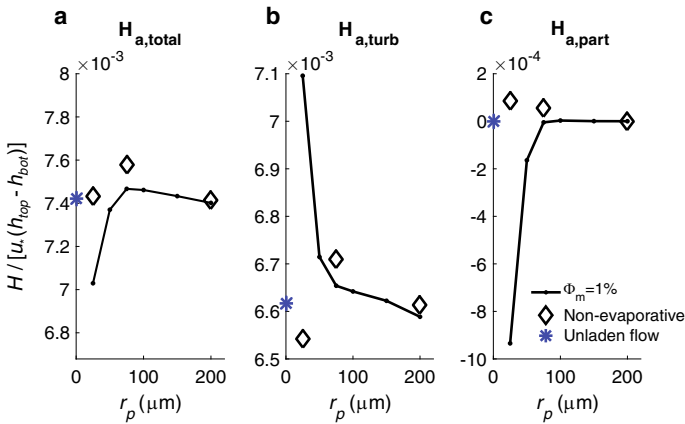


Fig. 6 Sensible-heat-flux components versus droplet radius extracted at $z = \delta/8$, compared with non-evaporative droplets (diamond), and unladen flow (blue asterisk). Components of the heat flux are normalized by the total enthalpy flux between two boundaries in z direction. **a** Total sensible heat flux $H_{a,\text{total}}$, **b** turbulent component of the sensible heat flux $H_{a,\text{turb}}$, **c** particle direct sensible flux $H_{a,\text{part}}$

reach without turbulent transport by our particle re-injection scheme. In a qualitative sense, this height is meant to mimic the so-called droplet evaporation layer (e.g. Andreas et al. 1995). The total enthalpy flux at $z = \delta/8$ increases with droplet radius and then exhibits a weak non-monotonic shape at large radius with a 1% mass loading. Additionally, the figure shows a limited modification with the largest change (decreasing by 2% from the unladen flow) occurring for the smallest droplets ($25 \mu\text{m}$). Note that, since the mass fraction is the same, smaller droplets are more numerous than are large droplets in the domain.

It is instructive, however, to look beyond the total enthalpy flux and consider the sensible and latent components individually. Figure 6 illustrates how the total sensible heat flux $H_{a,\text{total}}$ and its two dominant components $H_{a,\text{turb}}$ and $H_{a,\text{part}}$ vary with radius. Compared to the total heat flux shown in Fig. 5c, $H_{a,\text{total}}$ has a more pronounced non-monotonic trend with radius, where it has a peak around a radius of $100 \mu\text{m}$. The largest magnitude of modification compared to unladen flow is 5%, and the peak is 7% greater than the minimum at $25 \mu\text{m}$. We find that the turbulent and particle-induced components are also heavily influenced by droplet size, and that the modification becomes less sensitive above roughly $75 \mu\text{m}$. Comparing the sensible flux with its counterparts from non-evaporative droplets (hollow diamonds) with the same initial and boundary conditions, small evaporating droplets influence $H_{a,\text{turb}}$ and $H_{a,\text{part}}$ opposite to non-evaporating particles, highlighting the importance of evaporative cooling. However, larger droplets (e.g. $\geq 100 \mu\text{m}$) behave very similar to non-evaporating droplets (consistent with radius statistics shown in Fig. 4c); i.e., all three curves, especially $H_{a,\text{turb}}$, in Fig. 6 tend to converge towards the non-evaporative cases with increasing radius. This is in agreement with the results from Sect. 3.1.2 and Fig. 4a, and suggests that the sensible heat flux corresponding to large droplets is not sensitive to evaporation.

In the present system, vertical latent heat transfer dominates sensible heat transfer (see for example Fig. 5a, b), so Fig. 6 is only part of the story. Figure 7 therefore provides similar quantities as in Fig. 6 for latent heat flux components varying with droplet size. Compared to the pronounced modification in sensible flux, modification of total latent heat transfer (Fig. 7a) is not as large, ranging within 2% for all radii. The particle-induced latent flux $H_{q,\text{part}}$ converges to zero at large radii at the top of ejection layer, which is similar to

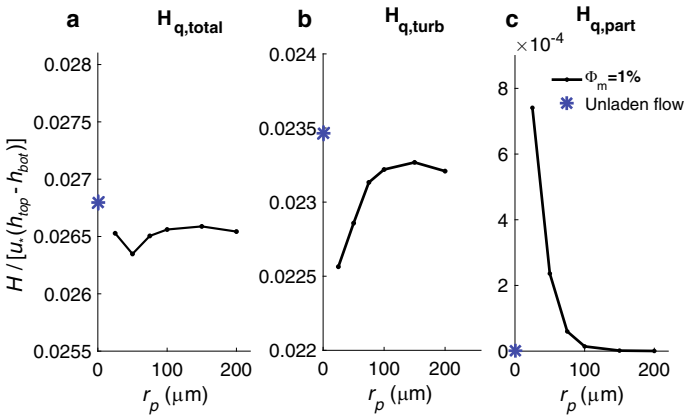


Fig. 7 Latent-enthalpy-flux components versus droplet radius, compared with unladen flow (blue asterisk) at the top of ejection layer ($z = \delta/8$). Components of heat flux are normalized by the total enthalpy difference between the two boundaries in the z direction. **a** Total latent heat flux $H_{q,total}$, **b** turbulent component of latent heat flux $H_{q,turb}$, **c** particle direct latent flux $H_{q,part}$

$H_{a,part}$. Likewise, we note that $H_{q,turb}$ generally increases with radius, but slightly decreases near $200 \mu\text{ m}$. We also find that the increase for $H_{q,turb}$ is of the same order of the decrease of $H_{q,part}$, which leads to the relatively flat curve in Fig. 7a.

The relation between $H_{q,turb}$ and $H_{q,part}$ demonstrates a cancellation between turbulent and particle-induced enthalpy fluxes. A similar result is found in Fig. 6 for $H_{a,turb}$ and $H_{a,part}$. In addition, the latent components evolve opposite to their sensible counterparts: the two particle-induced terms, $H_{q,part}$ and $H_{a,part}$, are of opposite sign, which indicates that droplets travelling upwards release moisture and cool the surrounding air, and the opposite is true for downward travelling droplets. We also find that $H_{q,turb}$ has a qualitatively opposite evolution with radius to $H_{a,turb}$. Similar evidence of this cancellation between latent and sensible heat fluxes has been documented in previous numerical studies (Fairall et al. 1994; Edson et al. 1996), where the decrease of sensible heat for droplet released at wave height offsets the increase of latent heat flux. In the current simulation, the multiple cancellation effects not only lead to an overall small enthalpy-flux modification, but also make the total enthalpy flux relatively insensitive to droplet radius (see Fig. 5b).

Therefore, we summarize that droplet size influences the balance of residence time scale (t_L) and thermodynamics time scale (τ_T or τ_r), which leads to a different combined behaviour, although the total modification on enthalpy flux is modest. We mainly focus on droplets in the small and large limits, because the transition between the two behaviours is relatively narrow. Small droplets with shorter thermodynamic response times have more flexibility to interact with the environment. Due to the longer suspension time, evaporative cooling of small droplets leads to a self-cancelling effect, where sensible and latent components of enthalpy flux are modified but compensated, yielding a limited total modification. Large droplets have ballistic inertial motions near the lower boundary and remain almost unchanged in temperature and radius, exhibiting different behaviour from small droplets. While each evaporating drop still releases a small amount of latent heat during the preliminary stage of evaporation (see Fig. 4d), the cumulative effect on the total latent enthalpy flux is trivial once averaged across the domain. This eventually leads to a very slight modification of the total enthalpy flux.

3.2 Influence of Mass Loading

In the previous section, the focus was mainly on the role of droplet radius on thermodynamic evolution and feedback at a fixed droplet loading $\Phi_m = 1\%$. We now comment on the influence of droplet mass loading by extending the mass loading of droplets to $\Phi_m = 5$ and 10% while boundary conditions remain the same. Three different radii are selected, 25, 75, and $200\ \mu\text{m}$, representing small, medium, and large droplets. We focus mainly on how the total enthalpy flux and its components change with increasing mass fraction.

Figure 8 displays the vertical profiles of the total enthalpy flux and its components for 25 and $200\ \mu\text{m}$ at $\Phi_m = 10\%$, as a counterpart of Fig. 5a, b at $\Phi_m = 1\%$. For H_{total} , large droplets provide a stronger modification than small droplets. The increase of large droplets is almost solely from the two turbulent fluxes, $H_{a,turb}$ and $H_{q,turb}$, and part of the latent enthalpy flux $H_{q,part}$ near lower boundary. However, in Fig. 8a for small droplets, all sensible and latent components are modified and continue to cancel each other, yielding a total enthalpy flux that remains nearly unchanged from both the unladen and $\Phi_m = 1\%$ cases. For example, Fig. 9 shows that this is generally true up to a mass loading of 10% , since in all cases the particle-flux components and the modifications to the turbulent fluxes all cancel each other.

Regarding the total heat flux H_{total} , large droplets tend to be slightly more sensitive to mass fraction, which is also shown in Fig. 9. In Fig. 9a, from $\Phi_m = 1$ to 10% , the magnitude of H_{total} increases by 6% for the $75\text{-}\mu\text{m}$ and $200\text{-}\mu\text{m}$ droplets but decreases by 1.6% for $25\text{-}\mu\text{m}$

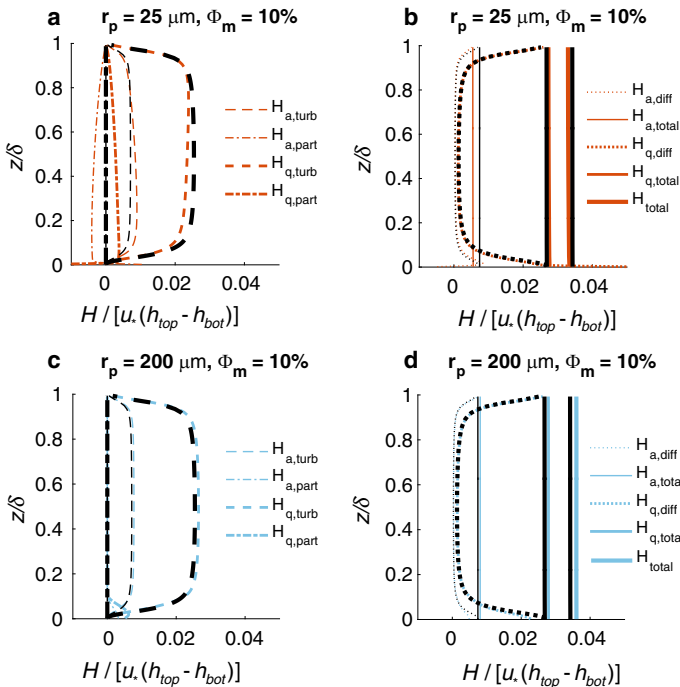


Fig. 8 Normalized total enthalpy flux H_{total} for a mass loading of $\Phi = 10\%$ for $25\text{-}\mu\text{m}$ case (brown), $200\text{-}\mu\text{m}$ case (blue) and unladen case (black). **a, c** Turbulent and particle enthalpy fluxes, and **b, d** diffusive and total enthalpy fluxes. Heat fluxes are normalized by the total enthalpy difference between the two boundaries in the z direction

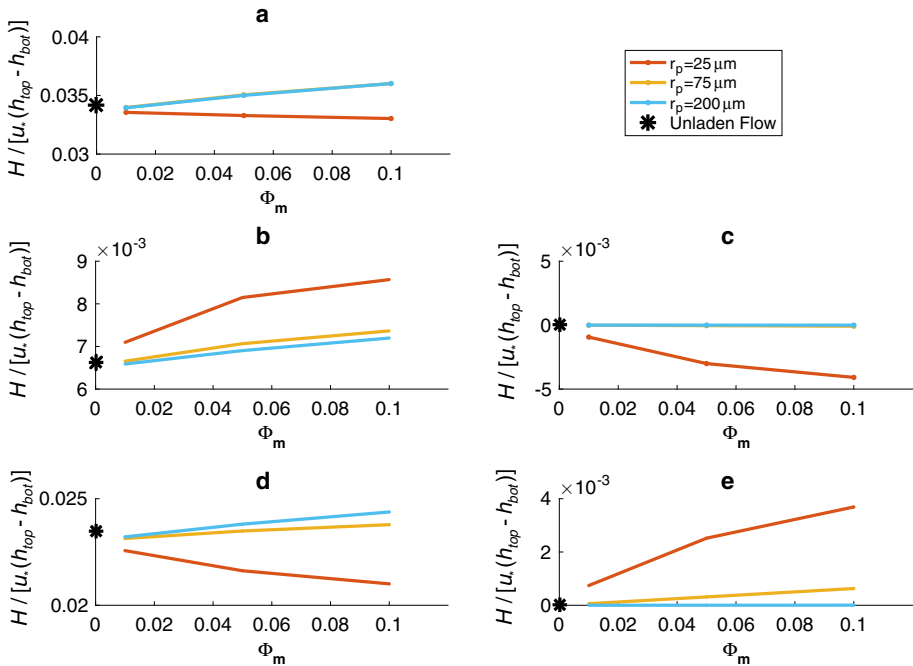


Fig. 9 Sensible and latent heat fluxes at a height of $z = \delta/8$ versus droplet mass fraction Φ_m , compared with unladen flow (blue asterisk): **a** total heat flux H_{total} , **b** turbulent component of sensible heat flux $H_{a,turb}$, **c** particle sensible heat flux $H_{a,part}$, **d** turbulent component of latent heat flux $H_{q,turb}$, **e** particle latent flux $H_{q,part}$. Note in (a) and (c), 75 and 200- μm have overlapped curves

μm droplets. However, Fig. 9c, e show that large droplets are insensitive to mass fraction for heat flux directly from the droplet feedback, $H_{a,part}$ and $H_{q,part}$. In particular, the sensible heat flux $H_{a,part}$ is insensitive to droplet mass fraction up to $\Phi_m = 10\%$ (note that 75 and 200 μm have overlapping curves). Considering that large droplets are confined within the ejection layer (as shown in Fig. 3) and have short lifetimes, the added contribution to the sensible heat flux does not cancel in the same way as for smaller droplets, which essentially do not participate in the evaporation process.

Therefore, the influence from mass loading is more important when considering heat flux from large droplets than from small droplets, though the flux modification for both small or large droplets at $\Phi_m = 10\%$ is still not very pronounced.

3.3 Influence of Boundary Conditions

Here, we probe the effect of boundary conditions in order to better characterize how well our idealized simulation set-up can be extended to more realistic conditions. Hence we systematically vary both the top and bottom temperatures and relative humidities; the details of the four different cases are given in Table 3 where the “Base” condition is the set-up in Table 2. The five boundary conditions represent different enthalpy gaps between the two boundaries distributed in various ways between sensible and latent heat. For example, case BCb would only yield a latent heat flux and no sensible heat flux since the top and bottom

Table 3 List of boundary conditions

| Group | T_{bot} (K) | T_{top} (K) | dT (K) | RH_{bot} (%) | RH_{top} (%) | dRH (%) |
|-------|---------------|---------------|----------|----------------|----------------|-----------|
| BCa | 304.15 | 301.15 | 3 | 100 | 90 | 10 |
| BCb | 301.15 | 301.15 | 0 | 100 | 90 | 10 |
| BCc | 301.15 | 296.15 | 5 | 100 | 90 | 10 |
| BCd | 301.15 | 298.15 | 3 | 100 | 80 | 20 |
| Base | 301.15 | 298.15 | 3 | 100 | 90 | 10 |

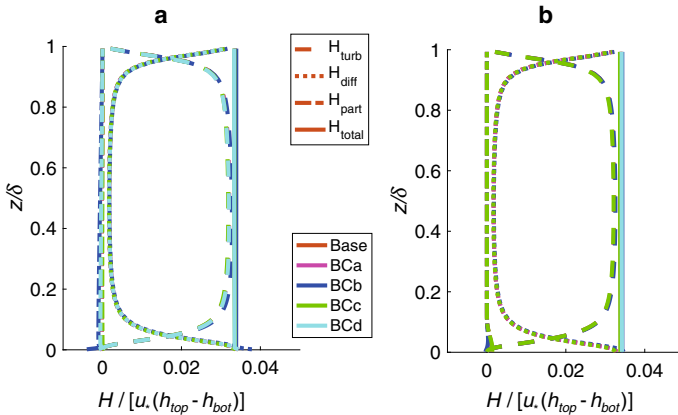


Fig. 10 Normalized vertical enthalpy flux for different boundary conditions. **a** Profiles of vertical enthalpy flux for 25- μm droplets. **b** Profiles of vertical enthalpy flux for 200- μm droplets. The colours are given in the legend. Here we combine the sensible and latent heat fluxes from the same physical mechanism as one term, e.g. $H_{turb} = H_{a,turb} + H_{q,turb}$, $H_{diff} = H_{a,diff} + H_{q,diff}$, etc. Note Lines not shown in the plot are overlapped with same terms for different boundary conditions. For all cases, $\Phi_m = 1\%$

temperatures are held equal. Similarly, we expect greater sensible heat transfer in group BCc than the Base group.

Figure 10 shows that regardless of the boundary conditions, however, when normalized by the total enthalpy difference between the top and bottom boundaries, the total enthalpy flux and its combined diffusive, particle-induced, and turbulent components remain nearly unchanged. This is likewise true for both small (Fig. 10a) and large (Fig. 10b) droplets, indicating that the consequent feedback of droplets from the thermodynamic evolution onto the surrounding flow identified in the previous sections is a robust effect that remains identical with changing boundary conditions (given proper normalization).

This insensitivity to boundary conditions, as with the influence of mass loading, is due largely to the aforementioned cancellation between the particle-flux components $H_{a,part}$ and $H_{q,part}$ and the modified turbulent fluxes $H_{a,turb}$ and $H_{q,turb}$. Figure 11 illustrates this cancellation effect for small droplets for the various boundary conditions. The modifications to sensible turbulent and particle-induced fluxes are in all cases offset by modifications to the latent turbulent and particle-induced fluxes, leading to an overall weak influence in total heat flux regardless of the boundary conditions.

Finally we note that the results presented herein are also insensitive to the initial droplet temperature ($T_{p,init}$). Small droplets, which experience the most complex thermodynamic

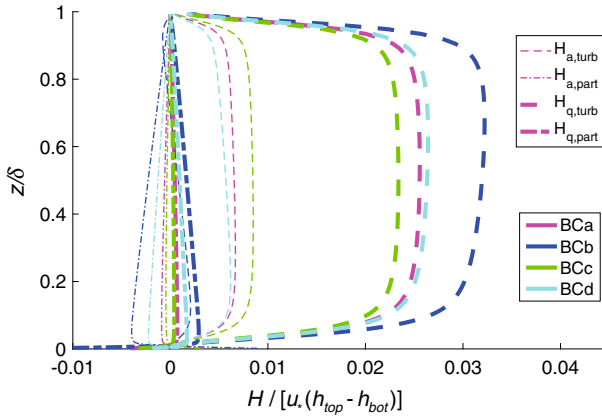


Fig. 11 Selected normalized components of sensible and latent heat flux, $H_{a,turb}$, $H_{a,part}$, $H_{q,turb}$, and $H_{q,part}$, for the four boundary conditions given in Table 3. Note $r_p = 25 \mu\text{m}$, $\Phi_m = 1\%$

evolution in the domain, quickly adjust to their surrounding temperature and therefore forget their initial value. This has been tested in the current set-up by manually changing the initial droplet temperature to be different than the bottom boundary temperature, and minimal changes were observed (not shown here). This is consistent with Mueller and Veron (2014a), who show that small droplets rapidly exchange heat before re-entering the ocean.

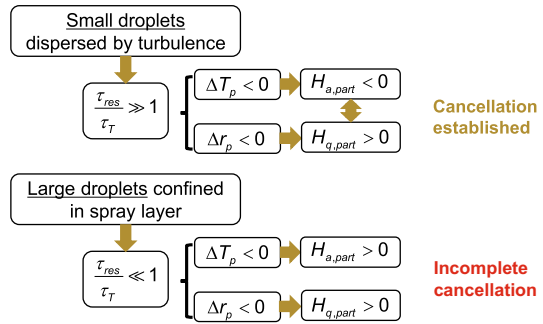
4 Conclusions

We investigated the feedback due to evaporating droplets in the turbulent marine atmosphere boundary layer (MABL) via idealized numerical simulations. Particularly we focused on how droplets modify the total heat/enthalpy transfer across the domain.

We observe that the feedback and evolutionary behaviour of droplets can be classified into two broad categories: “small” and “large” droplets, whose definitions are based on the balance between the droplet residence time and its thermodynamic time scales. Small droplets are more susceptible to entrainment into turbulent motions and transported throughout the domain and thus have a longer residence time, and at the same time have a more rapid thermodynamic response time than large droplets. This combination of scales for small droplets, however, leads to a cancelling feedback effect between modifications to sensible and latent heat fluxes, which results in a limited overall modification to the enthalpy flux across the boundary layer. Large droplets with longer thermodynamic time scales, however, do not have sufficient time to significantly change both temperature and radius. Therefore, large droplets behave somewhat as non-evaporating droplets, but also have small modifications to the total enthalpy flux. See Fig. 12 for a schematic.

While the direct numerical simulations performed are an idealized representation of the spray-laden MABL, we have demonstrated a robust insensitivity of this overall picture to both mass loading and boundary conditions. Increased mass loading affects small and large droplets slightly differently, since large droplets barely change the temperature and radius during evaporation and therefore have an incomplete feedback mechanism compared to the small droplets. Thus the influence of increasing mass loading is greater for larger droplets than it is for smaller ones. Likewise the boundary conditions do not affect the feedback due to

Fig. 12 A schematic of the influences of large and small droplets on particle-induced enthalpy



small droplets but only increase the magnitude of the individual terms that ultimately cancel one another.

In the context of spray modelling in the real MABL, we emphasize that feedback between droplet modifications to sensible and latent heat fluxes are critical if the overall affect of spray is to be modelled accurately. Our results show a qualitative difference from the significant increase of the total heat flux found in previous numerical studies (Andreas and Emanuel 2001; Mueller and Veron 2014b; Andreas et al. 2015), but this is perhaps due to the different coupling physics of droplets and turbulence. However, we found our results are in qualitative agreement with Edson et al. (1996) and Bianco et al. (2011) with respect to the cancellation effect and limited total flux modification. For small droplets that have the smallest thermodynamic response times, this feedback between their influence on sensible and latent heat fluxes could render them completely ineffective at increasing enthalpy fluxes from the ocean to the atmosphere. This is perhaps the reason why all existing observations (e.g. DeCosmo et al. 1996; Drennan et al. 2007; Zhang et al. 2008) at high wind speeds show no significant increase of heat-flux coefficients. Large droplets on the other hand, potentially enhance latent heat fluxes due to their incomplete evaporation cycle, but this enhancement is highly dependent on their concentration and suspension—physical processes that are not fully described in the present system.

Acknowledgements This work was supported by the National Science Foundation (NSF) under Grant No. AGS-1429921. The authors would like to thank the Computing Research Center at the University of Notre Dame for computational support. The authors would also like to acknowledge high-performance computing support from Yellowstone (UNDM0004), maintained by the Computational Information Systems Laboratory at the National Center for Atmospheric Research (NCAR). NCAR is supported by the NSF. To obtain digitized data of figures, please visit <https://curate.nd.edu/show/k930bv75t3z> (DOI: 10.7274/R01C1TT5).

References

- Andreas EL (1990) Time constants for the evolution of sea spray droplets. *Tellus B* 42:481497. doi:10.1034/j.1600-0889.1990.t01-3-00007.x
- Andreas EL (1992) Sea spray and the turbulent air-sea heat fluxes. *J Geophys Res* 97(C7):11,429–11,441. doi:10.1029/92JC00876
- Andreas EL (1995) The temperature of evaporating sea spray droplets. *J Atmos Sci* 52(7):852–862. doi:10.1175/1520-0469(1996)053<1634:COTOES>2.0.CO;2
- Andreas EL (2005) Approximation formulas for the microphysical properties of saline droplets. *Atmos Res* 75(4):323–345. doi:10.1016/j.atmosres.2005.02.001
- Andreas EL, Ka Emanuel (2001) Effects of sea spray on tropical cyclone intensity. *J Atmos Sci* 58(24):3741–3751. doi:10.1175/1520-0469(2001)058<3741:EOSSOT>2.0.CO;2

- Andreas EL, Edson JB, Monahan EC, Rouault MP, Smith SD (1995) The spray contribution to net evaporation from the sea: a review of recent progress. *Boundary-Layer Meteorol* 72(1–2):3–52. doi:[10.1007/BF00712389](https://doi.org/10.1007/BF00712389)
- Andreas EL, Persson POG, Hare JE (2008) A bulk turbulent air-sea flux algorithm for high-wind, spray conditions. *J Phys Oceanogr* 38(7):1581–1596. doi:[10.1175/2007JPO3813.1](https://doi.org/10.1175/2007JPO3813.1)
- Andreas EL, Mahrt L, Vickers D (2015) An improved bulk air-sea surface flux algorithm, including spray-mediated transfer. *Q J R Meteorol Soc* 141(687):642–654. doi:[10.1002/qj.2424](https://doi.org/10.1002/qj.2424)
- Bao JW, Fairall CW, Sa Michelson, Bianco L (2011) Parameterizations of sea-spray impact on the air-sea momentum and heat fluxes. *Mon Weather Rev* 139(12):3781–3797. doi:[10.1175/MWR-D-11-00007.1](https://doi.org/10.1175/MWR-D-11-00007.1)
- Bell MM, Montgomery MT, Emanuel KA (2012) Air-sea enthalpy and momentum exchange at major hurricane wind speeds observed during CBLAST. *J Atmos Sci* 69(11):3197–3222. doi:[10.1175/JAS-D-11-0276.1](https://doi.org/10.1175/JAS-D-11-0276.1)
- Bianco L, Bao JW, Fairall CW, Michelson SA (2011) Impact of sea-spray on the atmospheric surface layer. *Boundary-Layer Meteorol* 140(3):361–381. doi:[10.1007/s10546-011-9617-1](https://doi.org/10.1007/s10546-011-9617-1)
- Bukhvostova a, Russo E, Kuerten JGM, Geurts BJ (2014) Comparison of DNS of compressible and incompressible turbulent droplet-laden heated channel flow with phase transition. *Int J Multiph Flow* 63:68–81. doi:[10.1016/j.ijmultiphaseflow.2014.03.004](https://doi.org/10.1016/j.ijmultiphaseflow.2014.03.004)
- Clift R, Grace JR, Weber ME (1978) Bubbles, drops, and particles. Academic Press, New York
- DeCosmo J, Katsaros KB, Smith SD, Anderson RJ, Oost WA, Bumke K, Chadwick H (1996) Air-sea exchange of water vapor and sensible heat: the humidity exchange over the sea (HEXOS) results. *J Geophys Res Ocean* 101(C5):12,001–12,016. doi:[10.1029/95JC03796](https://doi.org/10.1029/95JC03796)
- de Leeuw G, Andreas E, Angelova M, Fairall C, Ernie R, O’Dowd C, Schulz M, Schwartz S (2011) Production flux of sea-spray aerosol. *Rev Geophys* 49(2010):1–39. doi:[10.1029/2010RG000349](https://doi.org/10.1029/2010RG000349)
- Drennan WM, Zhang JA, French JR, McCormick C, Black PG (2007) Turbulent fluxes in the hurricane boundary layer. Part II: latent heat flux. *J Atmos Sci* 64(4):1103–1115. doi:[10.1175/JAS3889.1](https://doi.org/10.1175/JAS3889.1)
- Edson JB, Fairall CW (1994) Spray droplet modeling 1. Lagrangian model simulation of the turbulent transport of evaporating droplets. *J Geophys Res* 99(C12):25,295–25,311. doi:[10.1029/94JC01883](https://doi.org/10.1029/94JC01883)
- Edson JB, Anquetin S, Mestayer PG, Sini JF (1996) Spray droplet modeling 2. An interactive Eulerian–Lagrangian model of evaporating spray droplets. *J Geophys Res* 101(C1):1279–1293. doi:[10.1029/95JC03280](https://doi.org/10.1029/95JC03280)
- Fairall CW, Kepert JD, Holland GJ (1994) The effect of sea spray on surface energy transports over the ocean. *Glob Atmos Ocean Syst* 2:121–142
- Fairall CW, Bradley EF, Hare JE, Grachev AA, Edson JB (2003) Bulk parameterization of air-sea fluxes: updates and verification for the COARE algorithm. *J Clim* 16(4):571–591. doi:[10.1175/1520-0442\(2003\)016<0571:BPOASF>2.0.CO;2](https://doi.org/10.1175/1520-0442(2003)016<0571:BPOASF>2.0.CO;2)
- Fairall CW, Banner ML, Peirson WL, Asher W, Morison RP (2009) Investigation of the physical scaling of sea spray spume droplet production. *J Geophys Res* 114(C10):C10001. doi:[10.1029/2008JC004918](https://doi.org/10.1029/2008JC004918)
- Helgans B, Richter DH (2016) Turbulent latent and sensible heat flux in the presence of evaporative droplets. *Int J Multiph Flow* 78:1–33. doi:[10.1016/j.ijmultiphaseflow.2015.09.010](https://doi.org/10.1016/j.ijmultiphaseflow.2015.09.010)
- Mueller J, Veron F (2010) A Lagrangian stochastic model for sea-spray evaporation in the atmospheric marine boundary layer. *Boundary-Layer Meteorol* 137(1):135–152. doi:[10.1007/s10546-010-9520-1](https://doi.org/10.1007/s10546-010-9520-1)
- Mueller JA, Veron F (2014a) Impact of sea spray on air-sea fluxes. Part I: results from stochastic simulations of sea spray drops over the ocean. *J Phys Oceanogr* 44:2835–2853. doi:[10.1175/JPO-D-13-0246.1](https://doi.org/10.1175/JPO-D-13-0246.1)
- Mueller JA, Veron F (2014b) Impact of sea spray on air-sea fluxes. Part II: feedback effects. *J Phys Oceanogr* 44:2835–2853. doi:[10.1175/JPO-D-13-0246.1](https://doi.org/10.1175/JPO-D-13-0246.1)
- Pruppacher HR, Klett JD (1997) *Microphysics of clouds and precipitation* (2nd ed.). Kluwer Academic Publishers, pp 509–511
- Ranz WE, Marshall WR (1952) Evaporation from drops: part 1. *Chem Eng Prog* 48(3):141–147
- Rastigejev Y, Suslov SA (2016) Two-temperature nonequilibrium model of a marine boundary layer laden with evaporating ocean spray under high-wind conditions. *J Phys Oceanogr* 46(10):3083–3102. doi:[10.1175/JPO-D-16-0039.1](https://doi.org/10.1175/JPO-D-16-0039.1)
- Richter DH (2015) Turbulence modification by inertial particles and its influence on the spectral energy budget in planar Couette flow. *Phys Fluids* 27:063304. doi:[10.1063/1.4923043](https://doi.org/10.1063/1.4923043)
- Richter DH, Sullivan PP (2014) The sea spray contribution to sensible heat flux. *J Atmos Sci* 71(2):640–654. doi:[10.1175/JAS-D-13-0204.1](https://doi.org/10.1175/JAS-D-13-0204.1)
- Richter DH, Bohac R, Stern DP (2016) An assessment of the flux profile method for determining air-sea momentum and enthalpy fluxes from dropsonde data in tropical cyclones. *J Atmos Sci* 73:2665–2682. doi:[10.1175/JAS-D-15-0331.1](https://doi.org/10.1175/JAS-D-15-0331.1)
- Russo E, Kuerten JGM, van der Geld CWM, Geurts BJ (2014) Water droplet condensation and evaporation in turbulent channel flow. *J Fluid Mech* 749:666–700. doi:[10.1017/jfm.2014.239](https://doi.org/10.1017/jfm.2014.239)

- Spalart PR, Moser RD, Rogers MM (1991) Spectral methods for the Navier–Stokes equations with one infinite and two periodic directions. *J Comput Phys* 96(2):297–324. doi:[10.1016/0021-9991\(91\)90238-G](https://doi.org/10.1016/0021-9991(91)90238-G)
- Thorpe SA (2005) *The turbulent ocean*. Cambridge University Press, Cambridge
- Veron F (2015) Ocean spray. *Annu Rev Fluid Mech* 47(1):507–538. doi:[10.1146/annurev-fluid-010814-014651](https://doi.org/10.1146/annurev-fluid-010814-014651)
- Veron F, Hopkins C, Harrison EL, Mueller JA (2012) Sea spray spume droplet production in high wind speeds. *Geophys Res Lett* 39:L16602. doi:[10.1029/2012GL052603](https://doi.org/10.1029/2012GL052603)
- Zhang JA, Black PG, French JR, Drennan WM (2008) First direct measurements of enthalpy flux in the hurricane boundary layer: the CBLAST results. *Geophys Res Lett* 35(14):2–5. doi:[10.1029/2008GL034374](https://doi.org/10.1029/2008GL034374)